Stationary Testing of a Pulse Tube Cryocooler Designed to Rotate at 6800 RPM with the Superconducting Rotor of an Electric Machine

William R. Sixel[1], Paul J. Passe[2], Aaron D. Anderson[1], Don Fong[1], Casey J. Theman[1], Justin J. Scheidler[1]

[1]NASA Glenn Research Center, Cleveland, OH, 44135, USA
[2]HX5, LLC, Brook Park, OH, 44142, USA

ABSTRACT

Electrified aircraft are being developed to increase the efficiency and reduce the cost of operating subsonic transport aircraft. Achieving a substantial impact necessitates focusing on single- and twin-aisle aircraft which use propulsion systems with >20 MW ratings. For these aircraft, multi-MW superconducting electric machines are being developed due to their high specific power and high efficiency. Most of these electric machines employ superconductors on their rotor, thereby requiring cryogenic cooling of the rotating system. An attractive solution is to conductively cool the rotor using a cryocooler that rotates with the rotor. NASA has been developing a 50 K pulse tube cryocooler for its High Efficiency Megawatt Motor (HEMM) that can operate while rotating at up to 6,800 rpm. The first non-rotating tests of the fully assembled HEMM cryocooler have been completed, and initial testing has yielded a no-load temperature of 112 K. A small helium leak into the vacuum system has been identified as the major bottleneck to performance, and based on measurements with the motor turned off there is an observed vacuum-side heat leak of approximately 30 W at 115 K. Immediate next steps for testing are to locate and mitigate the apparent helium leaks into the vacuum chamber. Thus far, compressor performance and the apparent heat lift after correcting for the heat leak are on par with expectations.

INTRODUCTION

Electrified aircraft propulsion (EAP) is a growing area of interest for a variety of economic, societal, and environmental reasons, including reduced fuel usage and strengthening the emerging electrified vertical takeoff market. EAP systems require high performance electric machines to be competitive with conventional engines. The use of superconductors has the potential to significantly improve the specific power and efficiency of high power electric machines. Superconducting wound-field machines are of particular interest for many applications from power generation to aviation because they nearly eliminate the rotor losses compared to conventional wound-field machines. Compared to permanent magnet rotors, superconducting rotors can have significantly higher specific power and efficiency. Fully superconducting motors are an active area of research, but a more mature technology that has been proposed is partially superconducting motors where only the rotor is superconducting [1]. NASA's High Efficiency Megawatt Motor (HEMM) is one such concept and is shown in Fig. 1 [2]. A key challenge in HEMM and similar

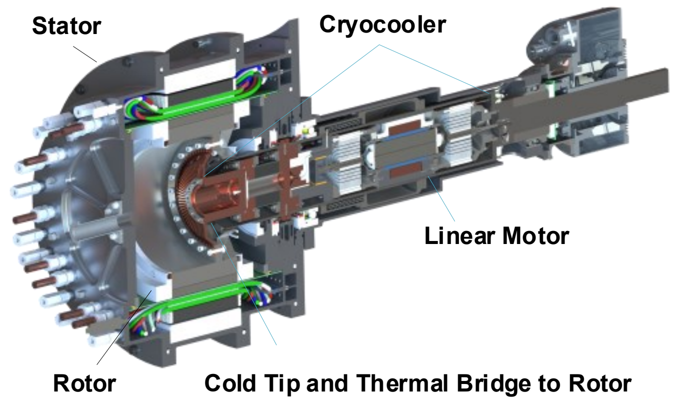

Figure 1. High Efficiency Megawatt Motor cross section, showing the rotating cryocooler integration.

machines is the cryogenic cooling of the rotor. In some concepts, a liquid or gaseous cryogen is passed through a rotating fluid coupling to cool the rotor. Helium recirculation systems have been designed for this purpose as one example [3]. Some key concerns with high speed fluid couplings are leakage, long-term robustness, and their losses which occur at cryogenic temperatures. In HEMM, instead the rotor is cooled by a cryocooler that is directly attached to the superconducting rotor. As a result, although HEMM uses superconductors, the interfaces to the aircraft are entirely conventional – only electrical interfaces and oil-based coolant. The efficacy of this approach was demonstrated on a stationary rotor using an off-the-shelf cryocooler [4]. This concept has also been previously developed by [5] in which a pulse tube cryocooler was developed, and also demonstrated recently by [6], [7] in which a free-piston Stirling cryocooler was used.

This paper presents the design and testing of the HEMM cryocooler. The design has been significantly refined since its conceptual design [8]. This Stirling pulse tube cryocooler was developed in-house at NASA Glenn Research Center. Development progressed in stages beginning with the fabrication of the linear motor. A revised linear motor was then built, and the cold head was developed in parallel. The revised linear motor underwent bench testing for static & dynamic performance as well as the calibration of the proximity probe. The first operational tests of the cryocooler have been completed, and preliminary test results are presented.

DESIGN OF THE HEMM CRYOCOOLER

Challenges of the Rotational Environment

Because the cryocooler must be designed to rotate coupled to the cryogenic rotor, this introduces several complications relative to a conventional stationary cryocooler. For example, there are additional mechanical loads on the pressure vessel that due to rotational body loads. If the thermal connection to the rotor is not carefully designed, there may be significant axial loads on the cold head due to the differential thermal expansion of the cryocooler and the shaft at cryogenic temperatures. Similarly, the thermal bridge between the cryocooler and rotor may also transmit a significant fraction of the motor torque through the cold head. Ideally, the thermal bridge is axially and torsionally compliant while still maintaining a good thermal connection. Waste heat rejection is more complex due to the rotation and high levels of compactness. While cryogenic rotary seals are eliminated by mounting the cryocooler to the rotor, HEMM's design still requires room temperature rotary coolant and vacuum seals. Many conventional cryocooler subcomponents are not necessarily designed to rotate. A free-piston design for example may encounter issues because any eccentricity of the cryocooler relative to the axis of rotation (which is controllable, but generally unavoidable) is a significant radial load on the gas bearings. Rotation may significantly alter the gas dynamics inside the cryocooler as well, due to centrifugal and Coriolis effects. Configuration trade studies led to the elimination of a free-piston design, the selection of a flexure bearing compressor, and a co-axial pulse tube geometry [8]. A cross section of the cryocooler is shown in Fig. 2.

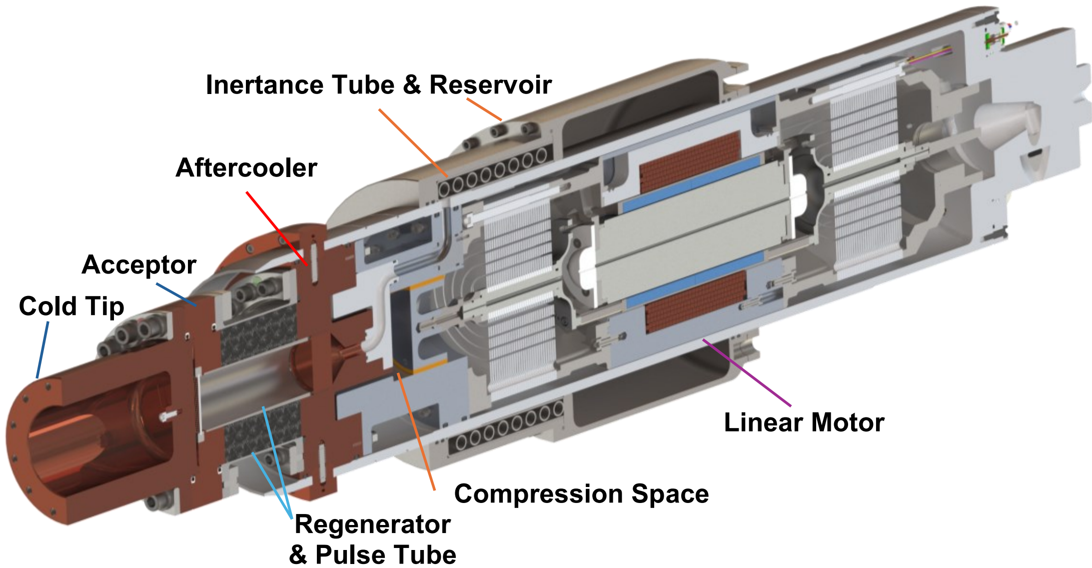

Figure 2. Cross section of the co-axial pulse tube cryocooler.

Cryocooler Detailed Design

The cryocooler design goals were to lift 50 W at 50 K using less than 2 kW of input electrical power while fitting within a 100 mm diameter shaft. The design was optimized using a specialized commercial software for modelling Stirling, Gifford-McMahon, and other periodic-flow thermodynamic devices [9]. The diameter constraint was challenging for the linear motor design as it constrained the diameter of the flexures, limiting the achievable stroke due to stress, and ultimately the air-gap diameter. Finite element analysis for mechanical stress and thermal performance was completed, and the results were incorporated into further optimizations of the cryocooler. These revisions focused on the pressure vessel and rotational stresses induced in the design; the design & conjugate CFD modeling completed for the cryocooler's cooling system; and the detailed electromagnetic & thermal analysis of the linear motor and testing of two prototypes [10], [11]. This testing demonstrated the performance of the prototype linear motors, their stable operation near resonance, and that they can survive at least 10^7 cycles.

Material selection for the cryocooler was critical, as common choices for cryogenics such as OFHC copper and 300-series stainless steels do not necessarily have sufficient strength to operate under the combined loads in the rotating cryocooler. Higher strength copper alloys were ultimately selected for several components at the cost of some lost thermal conductivity [12]. Zirconium copper has the added benefit of greater resistance to softening at elevated temperatures [13]. Ti-6Al-4V was used for several components for added strength and reduced heat leak, at the cost of more complex structural behavior due to its CTE mismatch to copper and stainless steel.

The higher pressure design of the HEMM cryocooler necessitated a random fiber regenerator [14] for its lower feature size due to the decreased thermal penetration depth [15] of a high pressure, high frequency cryocooler. Further, the random fiber design has the added benefit of increased specific surface area to increase heat transfer. Sintered random fiber filter stock media with 12 μm diameter 316L stainless steel fibers, and a nominal porosity of 75% was chosen as the base material, and the overall cryocooler design was re-optimized around this selection.

While the pulse tube eliminates any cryogenic moving parts, the co-axial configuration has a downside in that the interfaces to the pulse tube are not ideal for flow distribution. A well-functioning pulse tube has only axial temperature gradients, and ideally zero radial temperature gradients, as the pulse tube's only function is as a thermal buffer tube (an insulator between the warm and cold ends of the device). Any additional mixing increases heat leak from the warm to cold end and is undesirable. An unfortunate consequence of the co-axial configuration with an inertance tube is that the cold gas interface is at a larger radius than the pulse tube, and the warm interface (the inertance tube) is on the axis of symmetry. When centrifugal effects from rotation are introduced, the flow tends to stratify according to buoyancy gradients. This can cause extreme

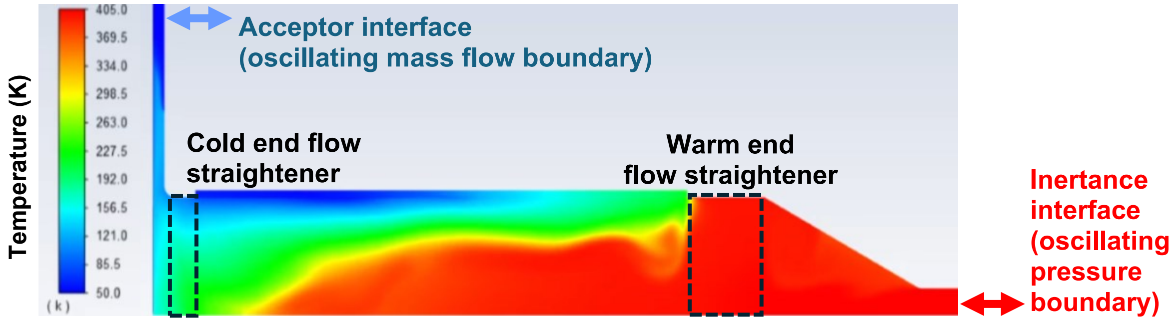

Figure 3. Snapshot from axi-symmetric, transient CFD of a thermally stratified pulse tube due to rotational body loads (6800 RPM). Severe maldistribution occurs due to undersized flow straighteners.

mixing if the flow straighteners are not sufficiently sized, so they must be significantly over-sized relative to conventional pulse tube designs. Further, the Coriolis effect adds additional complexity; the flow has a circumferential velocity as well, and the flow straighteners must accelerate the flow to the local circumferential velocity to prevent any additional mixing. During the design process, 2D axisymmetric CFD analysis was completed to try to specify an appropriate flow straightener design. Porous media models were used for the flow straighteners, calculating the appropriate input parameters from empirical correlations for screen media. This topic could be the subject of an entire paper, so for brevity only the result of a *poorly* behaving pulse tube with undersized flow straighteners is shown in Fig. 3. The stratification effects from rotation can be clearly noted, where the cold, higher density gas from the acceptor tends to stay close to the pulse tube wall and the jetting effect of the inertance tube is exacerbated because the warm, lower density gas tends to stay near the axis of symmetry. After the initial analysis, the flow straightener design was iterated to reduce the total heat leak & these changes were reflected in the cryocooler optimization model.

The compression space and piston interface was another particular concern, as the compressor performance is highly sensitive to piston blowby. A clearance design was chosen for simplicity and long-term reliability. The material of the piston and compression cylinder are matched for CTE effects. Additionally, the piston has a sleeve made from a low-friction PTFE blend to accommodate any dimensional mismatches and is intended to wear-in after thermal cycling.

After sizing the pulse tube flow straighteners, optimizing the cooling system, and selecting a regenerator stock material, the overall design was re-optimized for a wide set of parameters, including: frequency, charge pressure, regenerator outer diameter, pulse tube diameter, regenerator length, acceptor & aftercooler lengths, and the inertance tube length & diameter. The original design goals, as well as the optimized "realizable" design after the concerns were addressed, are listed in Table 1. During linear motor bench testing, several performance issues were identified: the force constant of the motor was considerably lower than predicted and the flexure springs had lower stiffness and greater nonlinearity than the design intent [11]. The predicted optimal operating point after considering the reduced linear motor performance is also listed in Table 1.

Cryocooler Thermal Management

The cooling system was also a challenge due to the competing design goals: 1) minimize aftercooler temperature, 2) minimize drag on the rotor, 3) minimize pumping power, 4) must function while the cryocooler is stationary and rotating, and 5) use the same coolant as the HEMM stator to reduce airframe interface requirements. The last point proved challenging as while PAO oil (MIL-87252 oil was chosen for the HEMM stator coolant) is an effective coolant relative to other dielectric fluids, it is considerably worse than a water-glycol mixture. The interaction of the first three design goals was captured in an optimization function to minimize total losses, in this case, 1) from the decreased efficiency caused by a higher heat rejection temperature, 2) from the calculated rotor drag, and 3) the fluid pressure drop and flow rate for a given design. Jet impingement cooling was selected due to the capability for very high heat transfer coefficients. The design was intended to operate with full flow at stationary startup, but optimized for minimized losses while rotating, where the heat transfer is enhanced by the rotation of the shaft

Table 1. Predicted Cryocooler Performance at Key Steps of the Design Process.

Parameter	Original Goal	Realizable Design	Weak Linear Motor
T_c (K)	50	50	50
T_h (K)	333	333	333
Lift (W)	50	28.8	9.8
Electrical Power (W)	< 2000	1792	949
Frequency (Hz)	60	57.1	53.4
Mean Pressure (MPa)	6.27	6.27	3.59
Displacement (mm)	13	12.5	11.6 (current limited)

and the flow rate can be reduced to reduce drag. The design was first optimized with empirical correlations for heat transfer and simple predictions for drag & pressure drop, which was later refined with detailed conjugate CFD modeling to more accurately predict performance.

The thermal management of the linear motor is another challenge as it is completely contained within the shaft and its losses are significant. There is no obvious method to directly remove losses from the linear motor, partially due to the location of the inertance reservoir on the outer diameter of the shaft that surrounds the motor. The chosen solution was to thermally couple the stator of the linear motor with the aftercooler by using heat pipes. Further, the heat pipes were slightly inclined to create a centrifugal component of acceleration in the direction of liquid flow between the heat pipe condenser and evaporator – therefore increasing their effectiveness when the rotor is spinning. This revolving heat pipe concept has been explored in the past [16], [17].

STATIONARY TESTING

There were a few design simplifications for stationary testing for cost, practicality, and schedule. The cold head assembly and linear motor are nearly unchanged from the design intent for the actual HEMM. The inertance tube and reservoir were simplified, such that the reservoir is not integral to the shaft but is instead a COTS 1.1 L gas bottle. The inertance tube is made from 5/16 in OD stainless steel tube made to the total length specification required. The rotary seals were replaced with static o-rings. A COTS vacuum chamber is used in place of the rotor vacuum housing, and a copper heater block with a cartridge heater is mounted to the cold tip to apply a known heat load. The heat pipes were omitted from the first installation of the cryocooler, and

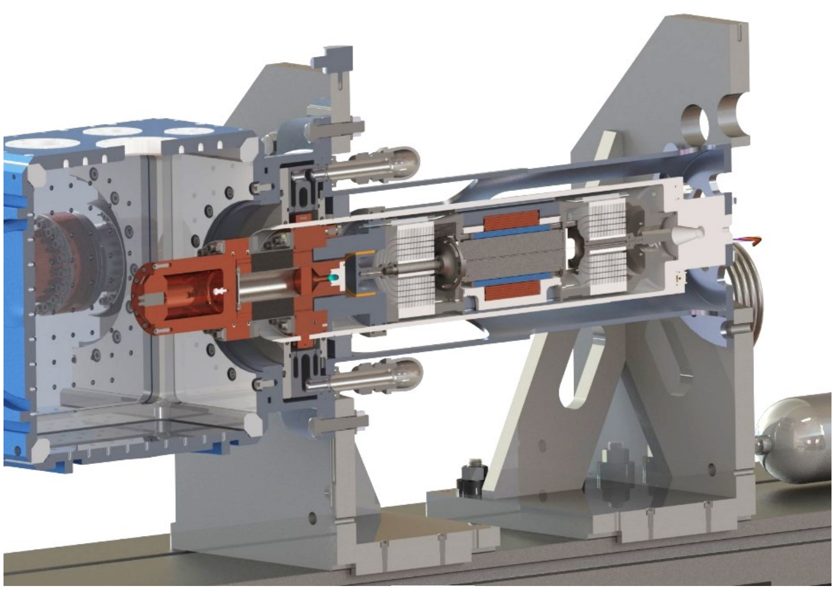

(a)

(b)

Figure 4. **(a)** Cross section of the cryocooler installed in the test stand with cooling system and vacuum chamber. **(b)** Photograph of the assembled cryocooler before installation into the shaft.

Table 2. Temperature and Pressure Instrumentation in the Cryocooler Stationary Test.

Temperatures		Pressures	
Cold Tip	Thin film resistance cryogenic temperature sensor	**Compression Space**	High frequency strain-gauge type pressure transducer
Cold Tip Heater Block		**Bounce Space**	
Aftercooler (2x)	Type E thermocouple	**Inertance Reservoir Mean Pressure**	High accuracy strain-gauge type pressure transducer
Linear Motor Coil	PT100 RTD	**Inertance Reservoir Dynamic Pressure**	Piezoelectric pressure transducer
Inertance Reservoir Inlet	Type T thermocouple	**Oil Inlet**	Strain gauge type pressure transducer
Cooling Oil Inlet		**Oil Outlet**	
		Vacuum Chamber	MEMS Pirani gauge

instead an air amplifier is used to cool the outside of the shaft and therefore the linear motor. The shaft is simplified, truncated on both ends, made from 17-4 PH stainless steel instead of Ti-6Al-4V, and does not have bearings (it is hard mounted to its housing). The cross section of the test setup and a photograph of the assembled cryocooler are shown in Figure 4. The measured mass of the photographed hardware was 22.9 kg, compared to the expected value from CAD of 23 kg.

Instrumentation, Data System, & Controls

The key instrumentation for temperature and pressure is listed in Table 2. The compression and bounce space pressures are measured by high frequency strain gauge pressure transducers and the housing of each of these is immersed in the bounce space. These transducers were selected for their high compactness. However, it was later discovered that the transducer housing is not hermetically sealed, so it developed a pressure offset while immersed in helium.

The linear motor displacement is measured by an eddy current proximity probe and tapered target. A fixture for the motor was designed to calibrate the displacement measurement statically, while installed in the linear motor, over the full displacement range. Motor input current and voltage are measured at the motor terminals. The heater power on the cold tip is also directly measured by a current probe and voltage taps. The motor is controlled by an AC power supply running in voltage & frequency control mode. The motor is essentially operated in open loop mode where the operator controls voltage and frequency to obtain the desired displacement amplitude and phasing between current and displacement, while also respecting thermal and current limits. The current is ideally controlled to have a phase lead of 90 degrees relative to displacement, as this is the definition of resonance and corresponds to maximum motor force at maximum piston velocity. In general, this maximizes compressor performance although small perturbations off this phasing could be beneficial for the thermoacoustics. All signals are logged continuously at 1 Hz. The high-speed signals are sampled at 50 kHz and displayed in the DAQ program. The high-speed signals can be saved on demand in a 1 s long snapshot. Those high-speed signals include the pressure signals, displacement, and motor terminal current and voltage measurements.

Initial Cooldown Results

After the cryocooler was fully assembled, it was taken through multiple evacuation, charging with helium, and re-evacuation cycles. No detectable leaks were observed during an operational pressure helium leak check at 2.75 MPa (400 psi). The cryocooler was under vacuum for about a week prior to the first operational cooldowns. The vacuum chamber was pumped down prior to operating the cryocooler until it reached 1e-3 Torr. Basic operational checkouts of the cryocooler were completed at 1 MPa charge pressure.

Three runs at 2 MPa, 2.5 MPa, and 2 MPa (repeat) charge pressures are plotted in Fig 5. The cooldown rate is limited by the large thermal mass of the cold tip, which is required for ideal steady state performance when cooling the superconducting rotor. Around 2 hours into run 2, the motor

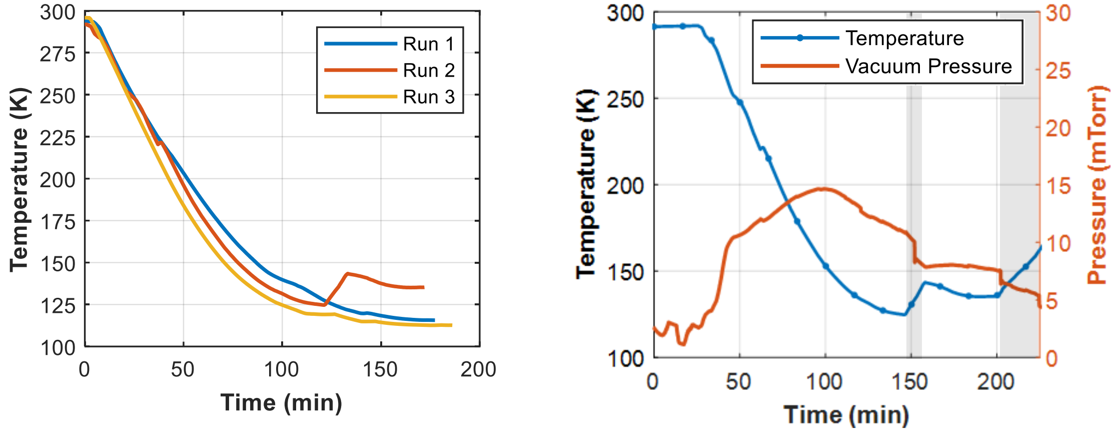

(a) (b)

Figure 5. (a) Cooldown curve for the first cryocooler operational tests. Runs 1 and 3 were at 2 MPa, and Run 2 was at 2.5 MPa. **(b)** Cooldown curve for run 2 with vacuum chamber pressure overlaid. Times when the motor was powered down are highlighted in grey.

was shut off for several minutes and then restarted to gain an estimate of the heat leak rate. Runs 1 and 2 were with no additional heat load on the cold tip. Run 2, at 2.5 MPa, did not reach as low of an ultimate temperature as run 1 despite higher pressure predicting better performance at this point. Run 3 has hold points at 120 K and 115 K where the cold tip heater was enabled and the net heat lift was measured. Additionally, it can be observed that the vacuum pressure is dynamic during the test. Notably, the vacuum pressure spikes when the motor is powered on. During run 2, it also measurably drops at ~120 min when the motor is temporarily powered off. The vacuum chamber pressure drops again when the motor is again turned off at ~200 min.

Overall, the high-speed data signals are working well. Examples are shown in Fig. 6. The data displayed is recorded near ambient temperature during the beginning of the cooldown. The compressor is seemingly performing well, obtaining a 1.35 pressure ratio at these conditions. A quick check of the pressure phasing is mostly as expected, with current peaking 90 degree before displacement (when displacement is zero) as intended. FFT's of the displacement and compression space pressures are plotted in Fig 7 (a) for the 115 K, 6 W heater input point. The harmonic content of the pressure in the compression space is significantly lower than that of the displacement signal. Only the first and second harmonics of the fundamental are significant in the pressure signal, whereas all observed harmonics in this frequency range are significant in the displacement. The phase between the pressure and displacement fundamentals is 48.1° at this condition, compared to an expected value of 47.4°. The pressure ratio decreased slightly to 1.33 relative to the startup condition. The observed compression space pressure fundamental amplitude of 251 kPa is also in good agreement with an expected value of 255 kPa. Comparing the reservoir pressure phasing to the compression space phase is also a good signal, as it shows the overall thermoacoustic system is behaving as expected and the inertance tube is appropriately sized. This observed phasing

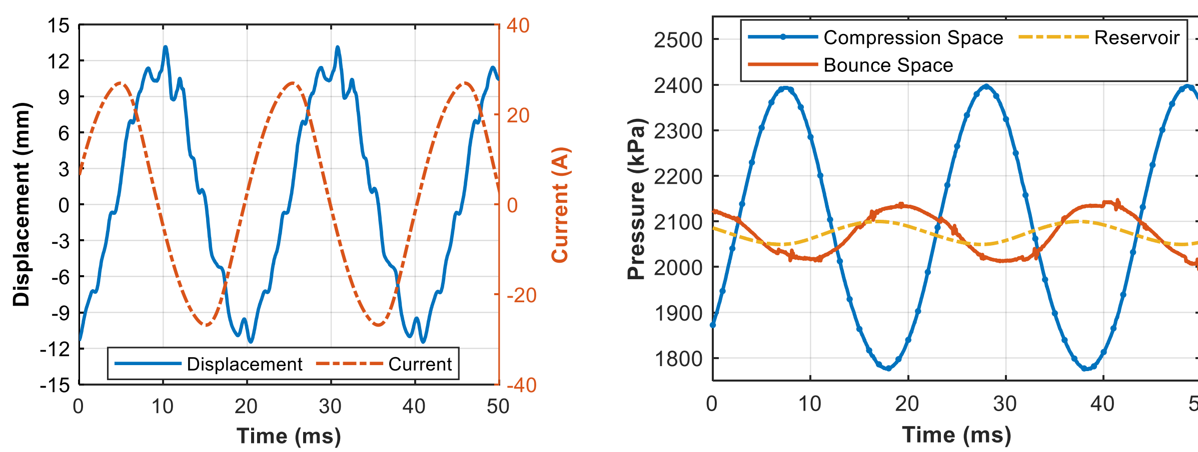

Figure 6. Sample of high-speed signals shortly after starting the cryocooler at ambient temperature.

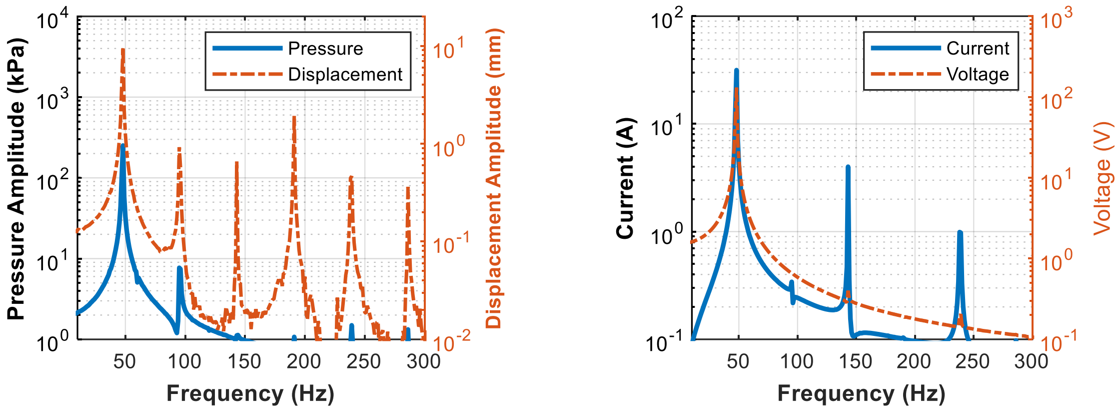

(a) (b)

Figure 7. Frequency domain amplitudes of the key high-speed signals while operating at 115 K.

between the compression space and the inertance reservoir is 167.2°, vs an expected value of 160.8°. Whereas the pressure amplitude of the reservoir exactly matches the predicted value of 19.2 kPa to within 3 significant figures. Since the reservoir is a dead end volume, this also directly relates to the flow rate into the reservoir [18]. With some additional thermoacoustic network analysis, the mass flow between the pulse tube and inertance tube can also be inferred from this [15]. The harmonics of the electrical signals are also displayed in Fig 7 (b). The voltage signal is extremely clean, only notably containing the fundamental frequency, which is consistent with the voltage-controlled power supply. The current has considerable odd harmonics of the fundamental at this operating point, which is consistent with the motor saturation behavior.

Estimated Heat Leak & Heat Lift

The large thermal mass of the cold tip permits its temperature response to be used to estimate the transient net lift and the total heat leak into the cryocooler. The mass of the heater block, cold tip, and acceptor is 4.8 kg of copper. The mass of the bolt pattern, nut blocks, and washers is 0.5 kg of stainless steel. The regenerator is neglected since it is not strongly conductively coupled. Temperature-dependent specific heat capacities are used to calculate the heat capacity of the cold head C (J/K). A weighted average of the measured heater block and cold tip temperatures is used to calculate temperature and its first derivative. The apparent net heat lift $\dot{q}_{net}$ (W) during transient and steady state points is defined in Equation 1. The sign of the second term is negative since the derivative of temperature is negative when the cryocooler is cooling down. When the cryocooler is operating, $\dot{q}_{net}$ represents the net heat lift from the cold head, neglecting any heat leaks. If the cryocooler is shut off, $\dot{q}_{net}$ becomes an approximation of the total heat leak into the cold head, internal and externally. Data from run 3 is used to calculate the values in Fig 8. The cryocooler starts up at an approximate net lift of ~80 W, decreasing with temperature. Two temperature holds at 120 K and 115 K with input heat load are present at ~120 min and ~160 min, respectively.

$$\dot{q}_{net} = \dot{q}_{heater} - C(T)\frac{dT}{dt} \tag{1}$$

Fig 8 (b) shows the rate of rise of temperature when the cryocooler is shut off near its no-load temperature. The motor was powered off at ~186 min and restarted at ~189 min, and the temperature rate of rise after internally equilibrating is used to estimate the heat leak at this temperature according to Equation 1. The apparent heat leak is the opposite of the apparent heat lift, which reaches its greatest value in Fig 8 (b) of approximately 45 W.

The cryocooler was warmed to ambient starting at ~205 min at an input heat load of 50 W as shown in Fig 8 (c). The heater load was increased to 100 W at ~220 min, which appears as a disturbance in the apparent lift curve. This data can be used to inform a corrected version of the actual lift vs temperature curve. From prior analysis, it was predicted that the cryocooler has approximately 15 W total internal heat leak at 50 K due to conduction in the regenerator and pulse tube walls, regenerator matrix, and the net pulse tube losses. For a conservative estimate, that

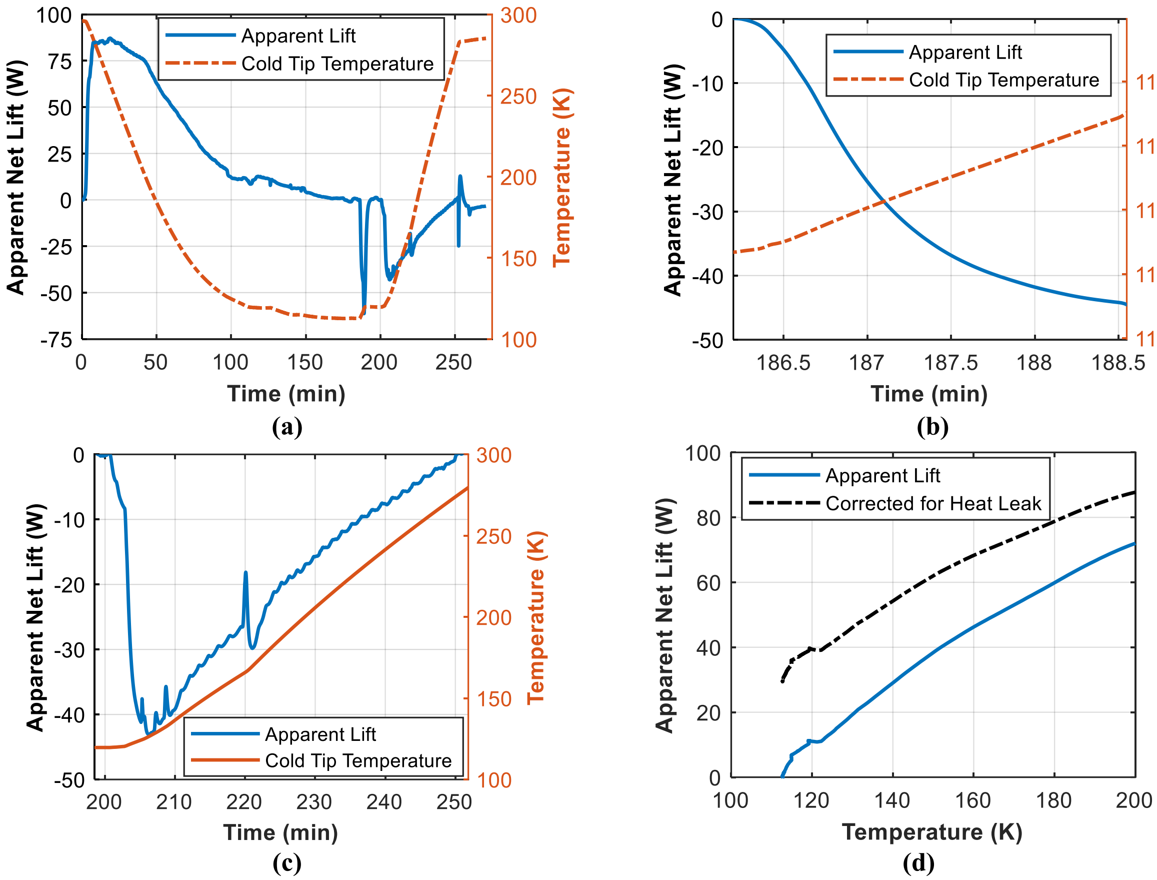

Figure 8. (a) Apparent heat leak calculated for run 3 at 2 MPa. (**b)** The motor was powered off temporarily at 186 min and the temperature rate of rise observed. **(c)** The apparent heat leak while heating to ambient temperature. **(d)** The measured lift vs cold tip temperature based on the cold head capacitance plus heater load, and after correcting for heat leaks.

predicted 15 W heat lift is subtracted from the observed total heat leak of 45 W at 115 K to obtain an estimated external heat leak of 30 W. This large external heat leak is due to the helium leak into the vacuum and the underperformance of the vacuum pump system. To better estimate the cryocooler performance, the heat load curve can be corrected. It is assumed for simplicity that the external leak rate varies linearly from 30 W at 115 K to 0 W at 293 K and this corrected leak curve is calculated by Eq. (2). The resulting data is plotted in Fig. 8 (d) vs cold tip temperature. The estimated total heat lift at 120 K of ~40 W aligns well with the predicted performance, after considering the reduced electromagnetic performance of the linear motor.

$$\dot{q}_{lift,corrected} = \dot{q}_{leak}(T) + \dot{q}_{heater} - C(T)\frac{dT}{dt} \tag{2}$$

DISCUSSION

The numerical model was not updated to match the exact operating conditions presented here, but initial correlations to the model appear favorable. For example, at a 2 MPa charge pressure, the predicted compressor performance and phasing of pressure and displacement, as well as compression space pressure and reservoir pressure, are quite close. The predicted net heat lift, after accounting for the apparent external heat loss, is within 10% of the expected value at 130 K. Overall, the thermoacoustics are operating close to predictions thus far, although considerable testing, data processing, and model correlation work remains.

Some nonlinearity can be seen in both the current and displacement which is consistent with past dynamic bench testing [11]. It is still unknown how much of the harmonics in the displacement signal is physical; as calibrated, the eddy current proximity probe uses a carrier frequency of ~700 kHz, far above the electrical fundamental of the motor. It is also observed through this test campaign thus far that the displacement signal harmonics worsen with both displacement amplitude (it is very sinusoidal at <5 mm amplitude) and current; 12 mm displacement amplitude at 2 MPa is a significantly noisier signal than the same displacement running at a lower pressure (and therefore motor current). It is also possible that mechanical dynamics are causing the issue. Any non-axial motion of the proximity probe or target can cause erroneous displacement signal. For example, vibration or fluid-structure interaction. The flow through the airgap of the motor and from the displacement of the flexures & moving magnet is not insignificant in the bounce space, so it is possible that the fluid dynamics may be contributing. A complicating factor is the non-linear spring stiffness which does predict that the motion profile may be very complex so some of this behavior may be actual piston motion.

The cryocooler not reaching as low of a temperature at 2.5 MPa vs 2 MPa was unexpected. The initial cooldown rate was higher, but the temperature plateaued sooner. The cryocooler was not re-evacuated between runs 1 and 2. An initial suspicion is that contaminants may have been present, possibly from out-gassing internally during the first run. Re-evacuating the cryocooler and re-pressurizing to 2 MPa for run 3 produced even better performance than run 1, which was also at 2 MPa. In part this was because a re-configuration of the vacuum pump system enabled a lower pressure in the vacuum chamber, but possibly lends credence to the contaminant hypothesis.

From the vacuum chamber pressure data, it is apparent that there is a small helium leak into the vacuum chamber. The leak rate tends to worsen with higher charge pressures and when the motor is running: the oscillating pressure seems to worsen the leak rate. Since these runs, a mass spectrometer helium leak detector was used with a sniffer probe to positively identify that the leak is at the acceptor-regenerator face seal. There are PTFE spring-energized face seals on the acceptor that will be disassembled, inspected, and replaced for future tests. However, the vacuum chamber pressure may still not be acceptable, so a larger pump may be required as well to further reduce the convective heat leak.

CONCLUSIONS & FUTURE WORK

While only the initial testing of the cryocooler has begun, the initial results are promising. The first runs of the cryocooler did not yield the intended target temperatures, this was seemingly due to small helium leaks and insufficient vacuum pumping. It is possible that larger than intended radiation heat leak is also present, so the addition of MLI is planned for future tests. Measurements of pressure and temperature are seemingly all working well, and dynamic measurements of pressure in the compression space and reservoir are very close to the expected value from analysis. After correcting for the additional heat leak, the apparent heat lift is also close to expectations.

Refinements of the data processing are planned for future testing. For example, the piston velocity can be estimated from motor data (force constant, inductance, and resistance) and an equivalent motor circuit model. Analysis of the motor and thermoacoustic performance data is still on-going, such as PV powers, compressor efficiency, etc. Immediate goals for the testing include the repair of the helium leak on the cold end and revisiting the vacuum chamber setup to achieve better vacuum. Future testing will include higher pressures, as better performance is predicted. Longer term goals may include a rotating test to quantify the cryocooler performance degradation with rotational speed. Other tests of interest include adding heat pipes coupling the linear motor to the aftercooler and long-term reliability testing. Revising the linear motor magnetic design would also be of considerable benefit. As the HEMM cryocooler has only a single compressor, it would benefit from a dynamic balancer, which would require modifications for integration.

ACKNOWLEDGMENT

This project is supported by the NASA Subsonic Vehicles Technologies and Tools project as part of the Advanced Air Vehicle Program. The authors would like to thank the projects' many contributors and supporters, including but not limited to, in alphabetical order: Joseph Assion, Joseph Connelly, Kirsten Duffy, Rodger Dyson, Frank Gaspare, Dave Hauser, Amy Jankovsky, Ralph Jansen, Susan Jansen, John Jones, Nathan Kleb, Amy Stalker, and Andy Woodworth.

REFERENCES

1. K. S. Haran *et al.*, "High power density superconducting rotating machines—development status and technology roadmap," *Supercond. Sci. Technol.*, vol. 30, no. 12, p. 123002, Dec. 2017, doi: 10.1088/1361-6668/aa833e.
2. R. Jansen *et al.*, "High Efficiency Megawatt Motor Preliminary Design," in *AIAA Propulsion and Energy Forum*, Indianapolis, IN, Aug. 2019. doi: 10.2514/6.2019-4513.
3. A. J. Caughley, N. Allpress, G. Lumsden, N. Rogers Rehn, M. Gschwendtner, and S. Jeong, "Cooling method for the rotor of a superconducting motor," *IOP Conf. Ser.: Mater. Sci. Eng.*, vol. 1301, no. 1, p. 012008, May 2024, doi: 10.1088/1757-899X/1301/1/012008.
4. J. J. Scheidler, E. J. Stalcup, T. F. Tallerico, W. Torres, K. P. Duffy, and T. T. Mulder, "Cryogenic vacuum chamber testing of a conductively-cooled, high temperature superconducting rotor for a 1.4 MW electric machine for aeronautics applications," *IOP Conf. Ser.: Mater. Sci. Eng.*, vol. 1302, no. 1, p. 012020, May 2024, doi: 10.1088/1757-899X/1302/1/012020.
5. Y. Kim, T. Ki, H. Kim, S. Jeong, J. Kim, and J. Jung, "High Temperature Superconducting Motor Cooled by On-Board Cryocooler," *IEEE Trans. Appl. Supercond.*, vol. 21, no. 3, pp. 2217–2220, Jun. 2011, doi: 10.1109/TASC.2010.2094597.
6. T. Balachandran *et al.*, "Superconducting Rotor With Closed-Loop Rotor-Mounted-Cryocooler: Design, Analysis, Assembly Procedure, and Experimental Results," *IEEE Trans. Appl. Supercond.*, vol. 36, no. 3, pp. 1–5, May 2026, doi: 10.1109/TASC.2025.3620773.
7. K. S. Haran *et al.*, "Aircraft Propulsion Motors With Cryogen-Free Superconducting Rotor," in *AIAA SCITECH Forum*, Orlando, FL, Jan. 2026. doi: 10.2514/6.2026-0999.
8. R. Dyson, R. Jansen, K. Duffy, and P. Passe, "High-Efficiency Megawatt Machine Rotating Cryocooler Conceptual Design," in *AIAA/IEEE Electric Aircraft Technologies Symposium*, Indianapolis, IN, USA, 2019. doi: 10.2514/6.2019-4515.
9. D. Gedeon, *Sage*. Gedeon Associates, Athens, OH. [Online]. Available: https://www.sageofathens.com/
10. K. P. Duffy, P. Passe, R. W. Dyson, Y. De Jesus-Arce, and A. D. Anderson, "Design, Analysis, and Testing of the HEMM Cryocooler Linear Motor," in *AIAA Propulsion and Energy Forum*, Aug. 2020. doi: 10.2514/6.2020-3601.
11. A. D. Anderson, W. R. Sixel, K. P. Duffy, and P. J. Passe, "Modeling and Testing of an Improved HEMM Linear Motor," in *IEEE International Electric Machines & Drives Conference*, Houston, TX, USA: IEEE, May 2025. doi: 10.1109/IEMDC60492.2025.11061092.
12. A. L. Woodcraft, "Zirconium Copper — a New Material for Use at Low Temperatures?," in *AIP Conference Proceedings*, Orlando, FL: AIP, 2006. doi: 10.1063/1.2355360.
13. de Groh, Henry C., III, D. L. Ellis, and W. S. Loewenthal, "Comparison of GRCop-84 to Other High Thermal Conductive Cu Alloys," NASA Glenn Research Center, Technical Memorandum TM-2007-214663, Feb. 2007. [Online]. Available: https://ntrs.nasa.gov/citations/20070017311
14. M. B. Ibrahim and R. C. Tew. Jr, *Stirling Convertor Regenerators*. CRC Press, 2012. doi: 10.1201/b11704.
15. G. W. Swift, *Thermoacoustics: A Unifying Perspective for Some Engines and Refrigerators*. Cham: Springer International Publishing, 2017. doi: 10.1007/978-3-319-66933-5.
16. T. A. Jankowski, "Numerical and Experimental Investigations of a Rotating Heat Pipe," University of New Mexico, Albuquerque, NM, 2007. doi: 10.2172/901587.
17. H. Hassan and S. Harmand, "An experimental work on the effect of the radius of rotation on the performance of revolving heat pipe (RVHP)," *Applied Thermal Engineering*, vol. 123, pp. 537–545, Aug. 2017, doi: 10.1016/j.applthermaleng.2017.05.133.
18. R. Snodgrass, V. Kotsubo, and J. Ullom, "Comparison of Three Methods for Oscillating Flow Measurements in Cryocoolers," in *Cryocoolers 23*, 2024.